Shifts in magnetic mineral assemblages support ocean deoxygenation before the end-Permian mass extinction

Check for updates

Min Zhang [1] ✉, Huafeng Qin[2,3], Yifei Hou[2,3], Kuang He[4], Chenglong Deng [2,3], Shu-Zhong Shen [5] & Yong-Xin Pan [1,3]

Expansion of oceanic anoxia is a prevailing hypothesis for driving the marine end-Permian mass extinction and is mainly based on isotopic geochemical proxies. However, long-term oceanic redox conditions before the end-Permian mass extinction remain unresolved. Here we report a secular redox trend based on rock magnetic experiments and cerium anomalies through the Changhsingian and across the Permian-Triassic boundary at the Meishan section, China. Magnetic mineral assemblages changed dramatically at ca. 252.8 million years age (Ma), which indicates that oceanic deoxygenation started about 0.9 million years earlier than the end-Permian mass extinction. The magnetite-dominant post end-Permian mass extinction interval suggests a ferruginous dysoxic conditions with enhanced weathering in the earliest Triassic. Also, a gradual magnetite abundance decrease to pre-extinction levels is observed at ca. 251.5 Ma, coinciding temporally with the waning of Siberian Trap and arc volcanism. All of these observations demonstrate that environmental deterioration began much earlier than the end-Permian mass extinction and finally collapsed in the end-Permian.

The end-Permian mass extinction (EPME) was marked by the loss of up to 81% of marine species in a short time interval of 61 ± 48 kyr and is considered the most severe biocrisis in Earth history[1–3]. Unraveling the mechanisms for this biocrisis is crucial for understanding the relationships between environmental changes and biological macroevolution. Numerous studies suggest that widespread marine anoxia likely drove the marine mass extinction[4–7]. A shift toward more dysoxic conditions at the EPME has been implicated in most global oceanic settings based on biomarkers[8], iron speciation[9,10], and geochemical and isotopic proxies[4,6,7,11]. Depending on their empirical calibration to modern marine sediments, these redox proxies provide understanding of significant insights into short-term redox history across the EPME. However, the long-term redox conditions remain undetermined.

Magnetite ($Fe^{2+}[Fe^{3+}]_2O_4$) and hematite ($[Fe^{3+}]_2O_3$) are commonly occurring magnetic minerals in sediments and rocks[12]. Magnetite has high saturation magnetization (M_s) that extends up to 92 Am^2/kg and low coercivity (H_c, ~10's of mT) at room temperature[13]. Hematite forms under oxidizing conditions and has a much lower M_s (0.4 Am^2/kg) than magnetite. Meanwhile, its H_c can be zero for superparamagnetic particles and up to 1000 s of mT for high coercivity pigments[13]. Previous studies indicated that magnetic mineral variations of terrestrial sediments (e.g., loess, red beds) are contributed to paleoclimatic patterns relating to rainfall and temperature[14,15]. Besides, a recent analysis of the 1.1 billion-year-old Paleolake Nonesuch sediments in North America has shown that redox processes are related to magnetite and hematite variations[16]. Likewise, the magnetic properties of eastern Mediterranean sediments provide evidence for a causal relationship between fluctuating redox conditions and the relative magnetic mineral assemblage[17]. Reductive dissolution may result in low magnetic mineral abundances and decreased particle size, leading to weakened magnetization and altered magnetic mineral assemblages. From these investigations, it is apparent that in some situation, accurately identifying the magnetic mineralogy of sediments may provide a useful tracer of paleo-oceanic redox conditions.

[1]Chinese Academy of Sciences (CAS) Key Laboratory of Earth and Planetary Physics, Institute of Geology and Geophysics, Chinese Academy of Sciences, Beijing 100029, China. [2]State Key Laboratory of Lithospheric Evolution, Institute of Geology and Geophysics, Chinese Academy of Sciences, Beijing 100029, China. [3]College of Earth and Planetary Sciences, University of the Chinese Academy of Sciences, Beijing 101400, China. [4]Frontiers Science Center for Deep Ocean Multispheres and Earth System, Key Lab of Submarine Geosciences and Prospecting Techniques, MOE and College of Marine Geosciences, Ocean University of China, Qingdao 266100, China. [5]State Key Laboratory for Mineral Deposits Research, School of Earth Sciences and Engineering and Environment and Frontiers Science Center for Critical Earth Material Cycling, Nanjing University, Nanjing 210023, China. ✉e-mail: zhangm@mail.iggcas.ac.cn

The renowned Meishan section (31°4.644′N, 119°42.510′E) was situated in the eastern Paleo-Tethys during the end-Permian to early Triassic[18] (Fig. 1a). It has been well studied for geochronology[1,19], multiple geochemical proxies[8,20,21], cyclostratigraphy[22], high-resolution biostratigraphy[23], and magnetostratigraphy[24], which provide a robust framework for correlation to other marine sections. In this study, we integrate mineral magnetism and microscopy to examine magnetic minerals combined with geochemical proxies through the Changhsingian and across the Permian-Triassic boundary (PTB) at the Meishan section to assess long-term redox conditions, associated with end-Permian deterioration and ecosystem collapse of a shallow marine environment and its early Triassic recovery.

Results

Magnetic mineral components

Hysteresis and isothermal remanent magnetization (IRM) results indicate the presence of mainly low- and high-coercivity magnetic minerals (Supplementary Fig. S1). Wasp-waisted loops indicate the presence of at least two magnetic phases (Supplementary Fig. S1c)[25]. Wide-open hysteresis loops likely indicate the presence of stable single-domain hematite (e.g., Supplementary Fig. S1i). Coercivity spectrum analysis of IRM acquisition curves[26,27] also reveals the presence of one or two components in limestone samples (Fig. 2): Component 1 with $B_{1/2}$ of 426–501 mT and a dispersion parameter (DP) of 0.28–0.33; Component 2 with $B_{1/2}$ of 31.6–55.0 mT and a DP of 0.35–0.60 (Supplementary Table S1). In addition, the relative proportion of each component changes synchronously with the S-ratio$_{0.3T}$ that calculated based on $0.5 \times (SIRM_{1T} - IRM_{-0.3T})/SIRM_{1T}$[28] (see the details in the Samples and Methods section). S-ratio$_{0.3T}$ values of > 0.97 indicate that Component 2 is the primary magnetic carrier, which has a granular morphology (Fig. 2d-f). Lower S-ratio values indicate an increasing proportion of Component 1 that consists of tabular Fe-oxide aggregates (Fig. 2a). Although large particles are often easily observed, experimentally determined magnetization and coercivity estimates reveal two distinct magnetic phases within the selected samples (Fig. 2 and Supplementary Fig. S1). The χ–T signal is weak in limestone samples, which prevents clear magnetic mineral identification.

From rock magnetic and SEM analyses, magnetic mineral assemblages in the Meishan section are dominated by high-coercivity component 1 (e.g., hematite, goethite) and low-coercivity component 2 (e.g., magnetite, maghemite). However, thermal demagnetization results for limestone samples indicate no noticeable remanent magnetization decrease at 80–150 °C[24], which excludes high-coercivity goethite and suggests the presence of hematite[12,29,30]. Usually, low-coercivity maghemite, which is cubic with inverse spinel crystal structures[31], coexists with magnetite in sediments. Nevertheless, magnetite is identified from low-temperature magnetic experiments through an apparent Verwey transition at 125 K for limestone samples[24], which is the main low-coercivity magnetic mineral (component 2). Thus, combining the rock magnetic and SEM results, low-coercivity magnetite and high-coercivity hematite are interpreted to be the main magnetic carriers in the Meishan section.

Magnetic Property Variations

Following magnetic parameter trends (Supplementary Table S2), the section can be divided into four intervals (Intervals I - IV in ascending order) with boundaries at ca. 252.8 Ma, ca. 251.9 Ma and ca. 251.2 Ma, respectively (Fig. 3). Anhysteretic remanent magnetization (ARM), M_s and H_{cr} variations suggest that the ferrimagnetic particle concentration fluctuates considerably in Interval I (ca. 253.8 – 252.8 Ma) (Fig. 3b-d). However, χ values (Fig. 3a) are nearly constant (-0.46 × 10^{-8} - 1.20 × 10^{-8} m^3/kg), probably due
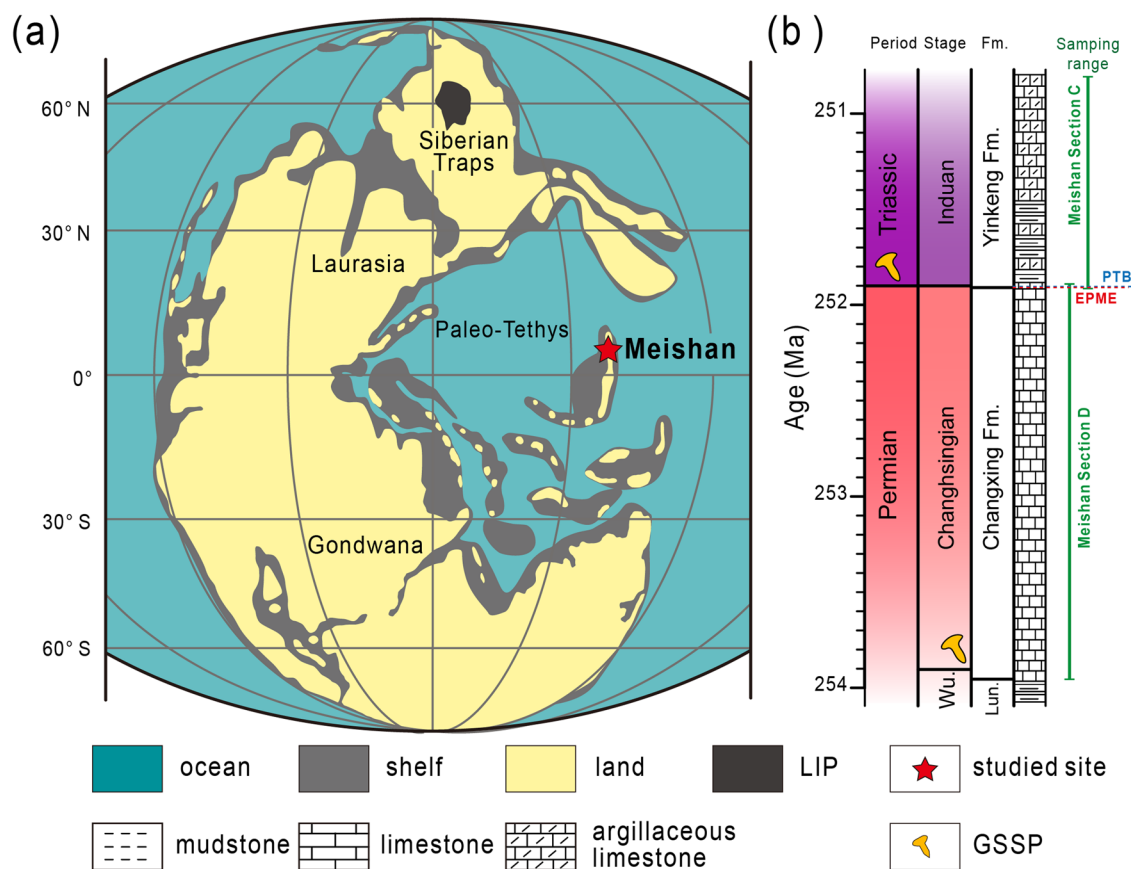
Fig. 1 | Locality map and end-Permian stratigraphy of the study section.
a Paleogeographic location of the Meishan section at the end-Permian (ca. 252 Ma) modified from ref.69. **b** Lithological column for the Meishan section and sampling range (green line). LIP, large igneous province. PTB, Permian-Triassic boundary. GSSP, Global Boundary Stratotype Section and Point. Wu., Wuchiapingian. Lun., Lungtan Formation. Fm., Formation.
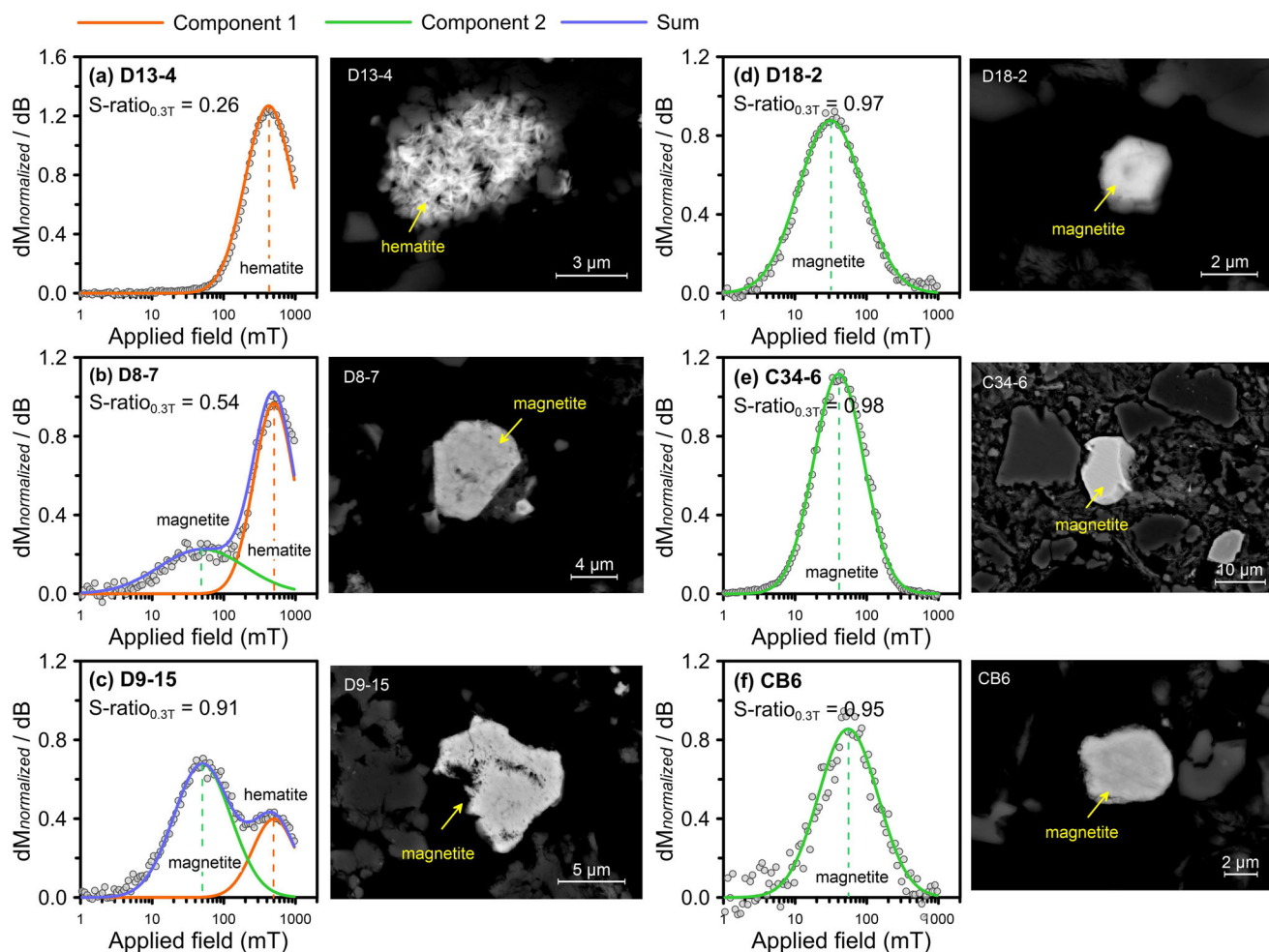
Fig. 2 | Mineralogy analysis results. Bulk coercivity spectrum, S-ratio$_{0.3T}$ and backscatter electron (BSE) micrographs of selected samples from the Meishan section, China. S-ratio$_{0.3T}$ = 0.5 × (SIRM$_{1T}$ - IRM$_{-0.3T}$)/SIRM$_{1T}$[28]. Samples shown in

Fig. 2**a-c** are from Interval I, whereas those displayed in Fig. 2**c-f** belong to the Interval II-IV, respectively. These sample positions have been marked in Fig. 3f using red dot symbols.

to dominant diamagnetic components (e.g., carbonate minerals). Moreover, the ARM to saturation isothermal remanent magnetization (ARM/SIRM$_{1T}$) ratio oscillates with an increasing trend in this interval, which reflects a magnetic grain size decrease (Fig. 3e). Additionally, S-ratio$_{0.3T}$ (0.26 - 1.00) fluctuations are associated with synchronous H$_{cr}$ (17.6 – 535.0 mT) and concentration-dependent magnetic parameter changes (Fig. 3c-f). Based on coercivity spectrum analysis (Fig. 2a-c), these variations are interpreted to indicate hematite and magnetite content changes in Interval I.

The S-ratio$_{0.3T}$ increases sharply at the end of Interval I (ca. 252.8 Ma) and then remains largely invariable with an average value of 0.98 to the top of the section; H$_{cr}$ also does not vary much (Fig. 3d, f). These parameters, coupled with IRM decomposition results and SEM observations (Fig. 2d-f), indicate that magnetite is the dominant magnetic carrier from Interval II to Interval IV. Furthermore, the ARM/SIRM$_{1T}$ ratio fluctuates with a decreasing trend, which indicates a magnetic mineral grain size increase in Interval II (Fig. 3e). In addition, χ, ARM and M$_s$ values rise gradually from the bottom of Interval III (ca. 251.9 Ma) and then decline in the middle-upper part of Interval III and return to stable values in Interval IV (ca. 251.2 Ma) (Fig. 3a-c). These oscillations indicate that the magnetite concentration first increases and then decreases in Interval III.
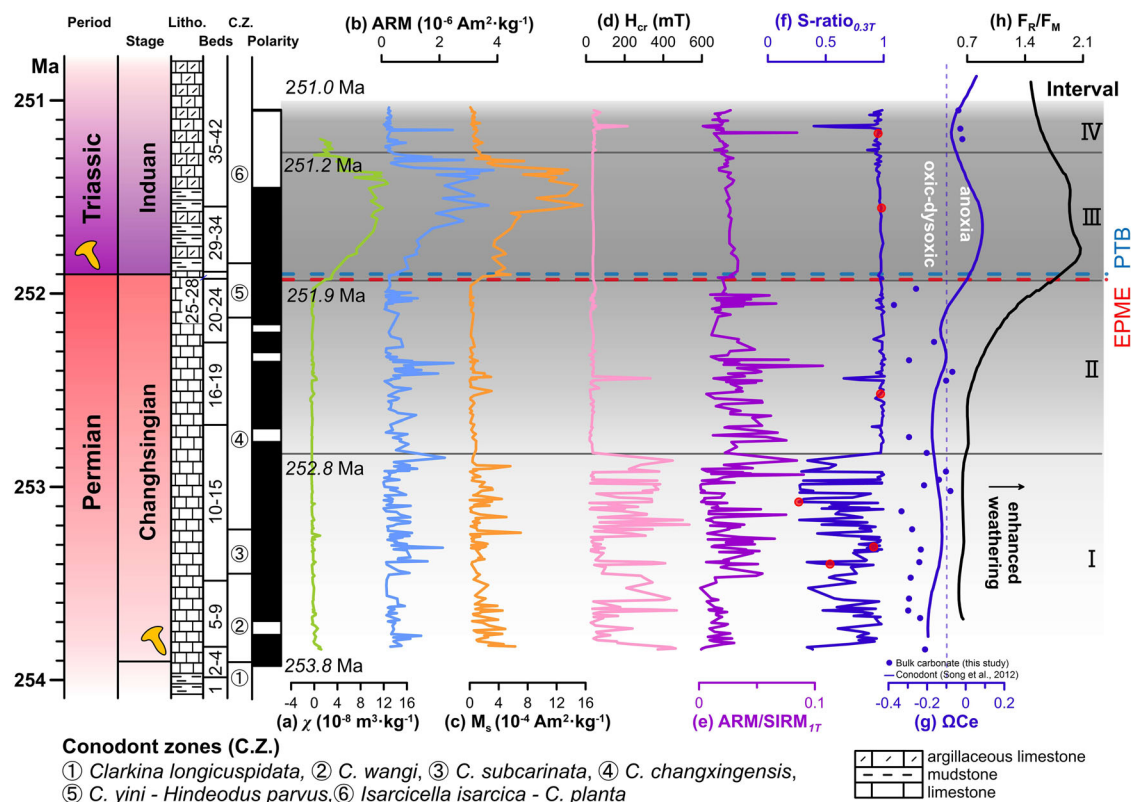
Cerium anomaly (ΩCe)

ΩCe values of bulk sample in the Meishan section range from −0.37 to 0.00 (Supplementary Table S3). They are less than -0.1 in Intervals I-II, indicating oxic-dysoxic conditions. ΩCe values fall into the anoxic range (> -0.1) in

Intervals III-IV. The ΩCe trend of bulk samples is consistent with published conodont ΩCe data[32] (Fig. 3g).

Discussion

Enhancement of chemical weathering

Magnetite in marine sediments generally originates from detrital inputs, bacterial activity (extracellular and intracellular), and authigenesis during diagenesis[33]. The different degrees of roundness and abrasion of the studied particles (Fig. 2) exclude an authigenic origin and indicate that the magnetite had a detrital origin. Also, paleomagnetic investigations confirm that magnetite at the Meishan section was deposited during limestone deposition[24]. Thus, magnetite concentration variations correspond to changes in continental silicate weathering and erosion. The lowest part of Interval III is dominated by mudstone. It is reasonable to expect that sili-ciclastic rocks would contain more abundant magnetite particles that were mostly reworked and transported. Rock magnetic parameters indicate that detrital magnetite concentrations started to increase at the Interval II-III boundary in the Meishan section (Fig. 3a-c), coinciding with a lithofacies change to high clay contents[34]. Meanwhile, the increasing of detrital magnetite content is consistent with major element Al variations at the Meishan[10]. Therefore, these magnetic minerals are related to lithologic types and are controlled by continental weathering. Notably, published lithium isotope data from the Meishan section reveal that the rate of chemical weathering rapidly increased ≥ 0.3 Ma before the main extinction event[21]. ^{87}Sr/^{86}Sr modeling for Meishan supports the interpretation that gradually

Fig. 3 | Rock magnetic parameters and geochemical proxies for the Meishan section. a–f Rock magnetic parameters. Red dots in (**f**) indicate the samples selected for coercivity spectrum analysis in Fig. 2. **g** Cerium anomalies (ΩCe), including bulk samples (blue dots, this study) and conodont samples (blue line)[32]. **h** Ratio of riverine to mantle Sr flux (F_R/F_M) to indicate weathering[35]. Conodont zones are from Yuan et al. [23]. The magnetic polarity sequence is from M. Zhang et al. [24]. χ, magnetic susceptibility. ARM, anhysteretic remanent magnetization. M_s, saturation magnetization. H_{cr}, coercivity of remanence. $SIRM_{1T}$, saturation isothermal remanent magnetization. S-ratio$_{0.3T}$ = 0.5 × ($SIRM_{1T}$ - $IRM_{-0.3T}$)/$SIRM_{1T}$[28]. Blue horizontal dashed line is the Permian-Triassic boundary (PTB); the red horizontal dashed line is the onset of the end-Permian mass extinction (EPME).

enhanced weathering started from the bottom of Interval II, and at the early Triassic continental weathering rates were intensified by a factor of >1.9 compared to those of the Late Permian (Fig. 3h)[35]. These slight differences in the onset of enhanced weathering may have been caused by different sampling densities, which need further investigation. Additionally, our data suggest that chemical weathering reached a maximum at ca. 251.5 Ma (Fig. 3a-c), synchronous with the waning of volcanic activity[36,37] and with a positive zinc isotope ($\delta^{66}Zn$) shift[20]. These processes probably delayed oceanic ecosystem recovery in the early Triassic after the mass extinction.

Latest permian qceanic anoxia and implications
Experimentally determined magnetization and coercivity estimates for samples indicated that magnetite and hematite were the main magnetic minerals before ca. 252.8 Ma (Interval I) and that magnetite then became dominant. The observed shifts in magnetic mineralogy were attributed to redox conditions or provenance dynamics. Notably, previous studies indicated that the Meishan section has not undergone later tectonic disturbances[38]. In addition, biostratigraphic and chemostratigraphic correlations corroborated the continuity of sedimentary deposition in the Meishan strata[23,37], denoting a notable absence of sedimentary hiatuses. These lines of evidence collectively suggest the stability in provenance within the Meishan section. Thus, the shifts in magnetic mineral assemblage are interpreted as being caused by the redox fluctuation, as indicated by the cerium-anomaly (ΩCe = Ce_N/($La_N^{0.5}$ × $Pr_N^{0.5}$)-1) geochemical proxy.

The ΩCe value, one of the most useful geochemical proxies available for gaining insights into local redox conditions[39], has been used for the Meishan section (Fig. 4g) to infer water-column anoxia throughout the late-Permian to early-Triassic[32]. The potential diagenetic alternation is a matter of significant concern across all carbonate samples. Luckily, lines of evidence

in accordance with previous studies indicate that rare earth element (REE) in carbonate rocks exhibit relative immobility during fluid-rock interaction. Additionally, they can uphold a seawater signature even after dolomitization, which predominant diagenetic process influencing carbonate rocks[40–42]. To limit the potential impact of post-depositional alternation and non-carbonate phase contamination on ΩCe, we applied filtering criteria to ΩCe data based on individual REE patterns and the correlations between of Y/Ho ratio and trace elements (e.g., Ti, Th, Cu, Sc) associated with diagenetic alternation[43,44]. Twelve samples with high Ti and Th contents or low Y/Ho ratio and five samples showed negative Eu anomalies indicate the influence of detrital contaminations or hydrothermal fluid-rock interactions[43–45] and were ruled out. Out of forty-one samples, twenty-four samples preserved the primary REE pattern and Ce anomalies (Supplementary discussion and Figs. S3–4). Both our new and published ΩCe data are generally inferred the Intervals I-II fall in an equivocal zone that could have been deposited under an oxygenated or dysoxic conditions[32]. The magnetic mineral assemblage changes from hematite mixed with magnetite to magnetite across the Interval I-II boundary (ca. 252.8 Ma) (Fig. 3), which indicates an oxic-dysoxic transition. Sediments in Interval I were oxic, which allowed preservation of detrital hematite and magnetite that is consistent with the magnetic observations. Also, the magnetic mineral in Interval II was dominated by magnetite, which indicated a non-sulfidic dysoxic condition[33]. Multiple S-isotopic evidence ($\delta^{34}S$ and $\Delta^{33}S$) also reflects that a lower degrees of sulphate reduction only episodically occurred at the top of Interval II (Beds 22-28)[5]. $^{87}Sr/^{86}Sr$ modeling for the Meishan section implies that gradually enhanced weathering started from Interval II (Fig. 3h), which led to the eutrophication and then resulted in dysoxic condition. From Interval III to Interval IV, the ΩCe values are higher than -0.1[32], indicating an anoxic depositional environment (Fig. 3g).

Fig. 4 | Compilation of redox proxy data and geological events across the end-Permian mass extinction (EPME). a Redox proxies, including magnetic minerals (this study), iron speciation[10], sulfur isotopes[5], thallium isotopes[7] and nickel isotopes[46]. **b** Volcanic activity: arc volcanism[37,54], coal fly ash[55], plume melting[56] and Siberian Traps[36]. **c** Species diversification rate[48]. **d** Carbon isotopes ($\delta^{13}C_{carb}$) from bulk carbonates[8].
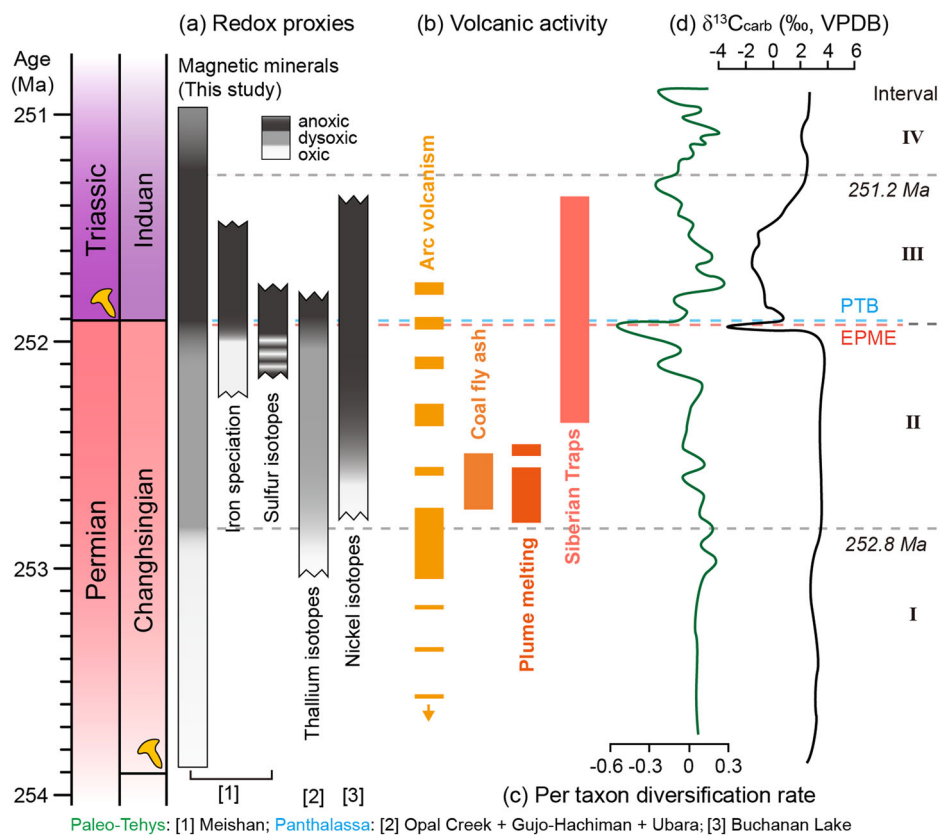
The anoxic condition is also evidenced by iron speciation[10] and biomarkers[8] in the Meishan section. The published iron speciation indicate nonsulfidic ferruginous conditions in the shallow water column based on the combination of $Fe_T > 0.5\%$, $Fe_{HR}/Fe_T > 0.38$ and $Fe_{py}/Fe_{HR} < 0.7$[10]. Ferruginous dysoxia prevailed but sulfide availability was restricted and was insufficient to sulfidize available reactive irons in Interval III–IV[10,33].

The observed long-term magnetic mineral shifts together with ΩCe values suggest that the onset of deoxygenation probably occurred before the EPME by ~0.9 Myr at the Meishan section (Fig. 4a), which is consistent with the published global geochemical redox proxies and biodiversity changes. For example, thallium isotope ($\varepsilon^{205}Tl$) profiles for the Gujo-Hachiman and Ubara sections range from -4.0 to -2.0, suggesting expansion of seafloor dysoxia by at least 1.0 Myr before the EPME[7]. Additionally, the nickel isotope data ($\delta^{60}Ni$) from Buchanan Lake indicate that deoxygenation occurred before the EPME by ~0.7 Myr[46] (Fig. 4a). The different onset age estimates for oceanic deoxygenation may be due to poor geochronologic constraints in these sections or to environmental difference at different locations. As a result, it is difficult to correlate precisely between the Meishan and other sections. However, despite the differences, these proxies were all potentially indicative of oceanic deoxygenation before the EPME. Also, the published paleontological data from the Meishan section indicate a species diversity decrease near the Interval I-II boundary[47]. Moreover, a similar biodiversification declined across South China and the northern peri-Gondwanan region suggested environmental deterioration ~1.2 Myr before the EPME[48] (Fig. 4c). Carbon isotopes ($\delta^{13}C_{carb}$) also show a subtle excursion[8] (Fig. 4d). Such deoxygenation events occurred over the prolonged end-Guadalupian biocrisis resulting in a gradual diversity decrease and selective extinction[49]. Interestingly, recent data from the terrestrial realm also indicated the extirpation of late Permian plant communities occurred some hundreds of thousands of years before the end-Permian[50–53].

Previous geochronological investigations have constrained that extensive arc volcanism occurred before 253 ± 0.5 Ma[37,54] and that Siberian plume melting launched at ca. 252.8 Ma[55,56] (Fig. 4b). Oceanic deoxygenation is temporally consistent with this volcanism (Fig. 4). The synchronization

indicates that early volcanic activity, which released volcanic volatiles and thermogenic gases[56], potentially contributed to the onset of ocean deoxygenation. Following major eruption sequences[36,37,57], the ocean became ferruginous anoxic.

While the existence of anoxic conditions before EPME is disputed, a combination of the published proxies provides conceptual insights in ocean redox evolution with synchronous volcanism during the late Permian Changhsingian (Fig. 5). Based on the presumed pathways, initial development of rising magma and plume melting at around 252.8 Ma probably contributed to the onset of oceanic deoxygenation[54,56] and led to upwelling of deep dysoxic water and allowed eukaryotic algae to proliferate[5,58], which developed a dysoxia condition in shallow marine waters. Massive volcanism also outgassed large amounts of CO_2 and SO_2 aerosols into the atmosphere[59], contributing to global hyperwarming and accompanying oceanic O_2 loss[60]. Moreover, this process caused rapid enhancement of chemical weathering from hot acid rain on freshly erupted lava. Enhanced chemical weathering brought soluble ions (e.g., Fe^{2+}, PO_4^{3-}, Ca^{2+} and Mg^{2+}) that increased nutrient fluxes to the ocean, leading to eutrophication[61]. Together, these processes led to widespread ocean dysoxia, which resulted in the EPME and delayed recovery of oceanic ecosystems.

Conclusion

Long-term magnetic mineral variations in the Meishan GSSP section may reveal a complex redox history during the EPME. Magnetic mineral assemblage variations record an onset of oceanic deoxygenation ~0.9 Myr before the EPME. The initial development of dysoxic water masses was detrimental to some life forms, which turned to widespread end-Permian anoxia, resulting in catastrophic extinction. This premature environmental deterioration may be considered a prelude to the impending mass extinction. Moreover, magnetite concentrations reveal that chemical weathering increase gradually over the EPME interval and decreased with the waning of volcanic activity. These records indicate that oceanic anoxia coupled with climatic changes played a crucial role in mass mortality and post-extinction recovery.
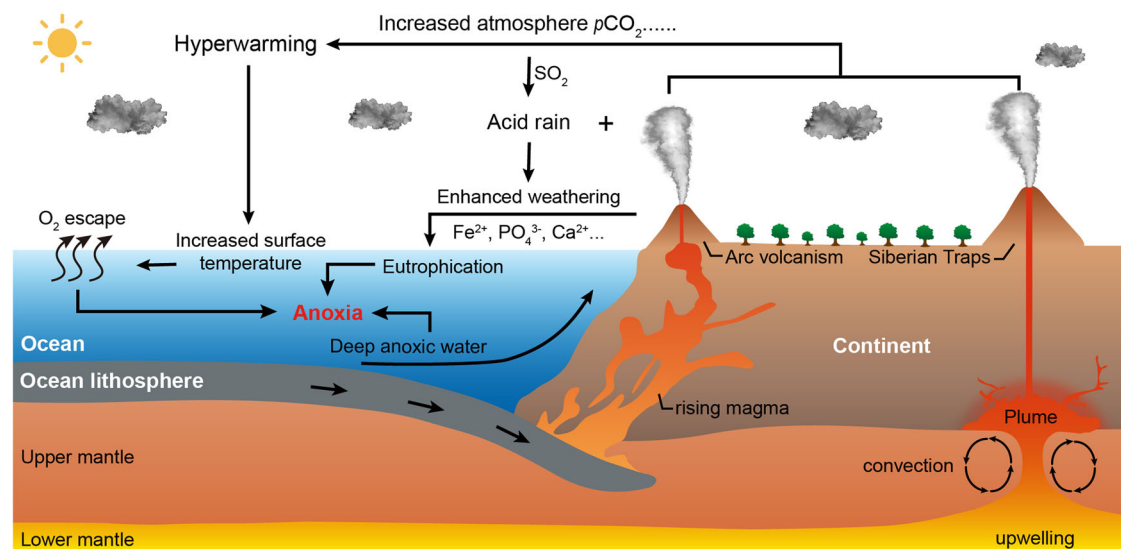
Fig. 5 | A Conceptual model for the end-Permian mass extinction (EPME) linked to environmental and climatic perturbations. The initiation of oceanic deoxygenation was triggered by the ascent of magma and mantle plume melting. Subsequent episodes of mass volcanism eruptions (e.g., Siberian Traps) and their relevant environmental impacts (e.g., global hyper-warming, oceanic O2 escape, eutrophication) contributed to widespread oceanic deoxygenation, ultimately resulting in the EPME.

Samples and methods

Samples

Two hundred sixty-four shallow-marine limestone samples were collected from the Meishan section, including 186 samples from the topmost Lungtan Formation to the Changxing Formation in Meishan section D and 78 samples from the Yinkeng Formation in Meishan section C (Fig. 1b). The average sampling interval was 10–15 cm, and all sample ages were computed using the Bchron software package[62,63] based on weighted mean radioisotope age estimates and their relative stratigraphic positions from the Meishan section[1,19]. Samples were broken into pieces (diameter ~5 mm) by hammer and were selected to avoid weathered surfaces and carbonate veins. Finally, the pieces were ground into powder using an agate mortar and pestle for magnetic measurements.

Rock magnetic measurements

Room-temperature hysteresis loops, isothermal remanent magnetization (IRM) acquisition curves and DC demagnetizations of IRM were measured using a Princeton Measurements Corporation vibrating sample magnetometer (VSM3900, sensitivity: 5×10^{-10} Am^2). Hysteresis parameters, such as M_s, saturation remanent magnetization (M_r), H_c and the coercivity of remanence (H_{cr}), were obtained. IRM acquisition curves were smoothed using the Savitzky-Golay algorithm before coercivity spectrum analysis[26,27]. Magnetic susceptibility (χ) and high-temperature magnetic susceptibility (χ–T) were measured using an MFK1-FA Kappabridge system (AGICO Ltd., Brno). An anhysteretic remanent magnetization (ARM) was imparted to samples in a 0.05 mT DC field superimposed on a peak alternating field of 100 mT and measured with a 2G-Enterprises Model 760 cryogenic magnetometer (sensitivity: 5×10^{-11} Am^2). A saturation IRM (SIRM) was imparted in a 1 T applied field using an MMPM10 pulse magnetizer, followed by the application of a 0.3 T backfield magnetization. The corresponding remanence was measured, termed SIRM$_{1T}$ and IRM$_{-0.3T}$, respectively. The S-ratio$_{0.3T}$ was calculated as $0.5 \times$ (SIRM$_{1T}$ - IRM$_{-0.3T}$)/SIRM$_{1T}$[28].

Scanning electron microscope analysis

Selected fresh samples were ground into powder using an agate mortar and pestle and were then dissolved into a mildly acidic buffer solution (pH~4) for 2-3 days to beneficiate the trace concentration of magnetic minerals in limestone samples. The buffer solution was made of 2 M acetic acid (CH$_3$COOH) and 1 M sodium acetate (NaCH$_3$COOH) at a 4:1 ratio[64]. Then, residual extracts were prepared for scanning electron microscope (SEM) observations. Backscattered electron (BSE) images and SEM-based energy-dispersive X-ray spectroscopy (EDXS) micro-analyses were obtained for eight samples with a Zeiss (Germany) field emission SEM (Gemini 450) at a 15 kV accelerating voltage and 2 nA current with a working distance of ~10 mm.

Cerium anomaly measurements

Forty-one bulk samples through the entire Meishan section were selected for cerium anomaly analysis following the protocol described in Jenner et al.[65]. All samples were powdered into <75 μm using an agate TEMA mill after removal of the weathered surfaces and secondary veins. Subsequently, 50 mg of each powdered sample underwent dissolution in sub-boiling distilled HF, followed by evaporation to incipient dryness at 150 °C to eliminate the silicate. The resulting residuals were further dissolved in a mixture of sub-boiling distilled HF and HNO$_3$ in a high-pressure Teflon bomb, allowing for a thorough digestion process lasting 96 h at 190 °C. After evaporation of the HF-HNO$_3$ mixture, the sample was solubilized in HNO$_3$, evaporated to dryness, taken up in 2-3 ml of HNO$_3$, transferred to a 50 ml centrifuge tube and diluted to a final volume of 50 ml. Meanwhile, 1 ml 500 ng/g Rh was added to each sample as an internal standard for correcting matrix effects and instrument drift for measurements. The analyses were performed with an Agilent 7500 inductively coupled plasma mass spectrometer (ICP-MS) (USA) at the Beijing ZKKY GeoAnalysis Laboratory Co., Ltd. (Beijing, China). Analytical errors were better than ± 5% for most elements based on USGS standards and two Chinese national standards (GBW07107, GBW07108).

The rare earth elements (REE) were normalized to Post Archean Australian Shale (PAAS)[66,67]. Cerium anomalies (ΩCe) were calculated using the formula Ce$_N$/(La$_N^{0.5} \times$ Pr$_N^{0.5}$)-1[68] and subsequently integrated with previously published in-situ ΩCe of conodont at the Meishan section[32].

Data availability

All supplementary data related to this paper are available at https://doi.org/10.5281/zenodo.10851614.

References

1. Burgess, S. D., Bowring, S. A. & Shen, S. Z. High-precision timeline for Earth's most severe extinction. *Proc. Natl. Acad. Sci. USA* **111**, 3316–3321 (2014).
2. Fan, J. X. et al. A high-resolution summary of Cambrian to Early Triassic marine invertebrate biodiversity. *Science* **367**, 272–277 (2020).
3. Stanley, S. M. Estimates of the magnitudes of major marine mass extinctions in earth history. *Proc. Natl. Acad. Sci. USA* **113**, e6325–E6334 (2016).
4. Fang, Z. et al. Ocean redox changes from the latest Permian to Early Triassic recorded by chromium isotopes. *Earth Planet. Sci. Lett.* **570**, 117050 (2021).
5. Shen, Y. et al. Multiple S-isotopic evidence for episodic shoaling of anoxic water during Late Permian mass extinction. *Nat. Commun.* **2**, 1–5 (2011).
6. Zhang, F. et al. Congruent Permian-Triassic δ238U records at Panthalassic and Tethyan sites: Confirmation of global-oceanic anoxia and validation of the U-isotope paleoredox proxy. *Geology* **46**, 327–330 (2018).
7. Newby, S. M., Owens, J. D., Schoepfer, S. D. & Algeo, T. J. Transient ocean oxygenation at end-Permian mass extinction onset shown by thallium isotopes. *Nat. Geosci.* **14**, 678–683 (2021).
8. Cao, C. et al. Biogeochemical evidence for euxinic oceans and ecological disturbance presaging the end-Permian mass extinction event. *Earth Planet. Sci. Lett.* **281**, 188–201 (2009).
9. Grice, K. et al. Photic zone euxinia during the Permian-Triassic superanoxic event. *Science* **307**, 706–709 (2005).
10. Xiang, L. et al. Oceanic redox evolution around the end-Permian mass extinction at Meishan, South China. *Palaeogeogr. Palaeoclimatol. Palaeoecol.* **544**, 109626 (2020).
11. Elrick, M. et al. Global-ocean redox variation during the middle-late Permian through Early Triassic based on uranium isotope and Th/U trends of marine carbonates. *Geology* **45**, 163–166 (2017).
12. Jiang, Z. et al. The magnetic and color reflectance properties of hematite: From Earth to Mars. *Rev. Geophys.* **60** https://doi.org/10.1029/2020rg000698 (2022).
13. O'Reilly, W. *Rock and Mineral Magnetism*. (Springer, Boston, MA., 1984).
14. Lepre, C. J. & Olsen, P. E. Hematite reconstruction of Late Triassic hydroclimate over the Colorado Plateau. *Proc. Natl. Acad. Sci.* **118**, e2004343118 (2021).
15. Deng, C., Shaw, J., Liu, Q., Pan, Y. & Zhu, R. Mineral magnetic variation of the Jingbian loess/paleosol sequence in the northern Loess Plateau of China: Implications for Quaternary development of Asian aridification and cooling. *Earth Planet. Sci. Lett.* **241**, 248–259 (2006).
16. Slotznick, S. P., Swanson-Hysell, N. L. & Sperling, E. A. Oxygenated Mesoproterozoic lake revealed through magnetic mineralogy. *Proc. Natl. Acad. Sci. USA* **115**, 12938–12943 (2018).
17. Larrasoaña, J. C., Roberts, A. P., Stoner, J. S., Richter, C. & Wehausen, R. A new proxy for bottom-water ventilation in the eastern Mediterranean based on diagenetically controlled magnetic properties of sapropel-bearing sediments. *Palaeogeogr. Palaeoclimatol. Palaeoecol.* **190**, 221–242 (2003).
18. Wu, L., Kravchinsky, V. A. & Potter, D. K. Apparent polar wander paths of the major Chinese blocks since the Late Paleozoic: Toward restoring the amalgamation history of east Eurasia. *Earth Sci. Rev.* **171**, 492–519 (2017).
19. Shen, S. Z. et al. Calibrating the end-Permian mass extinction. *Science* **334**, 1367–1372 (2011).
20. Liu, S. A. et al. Zinc isotope evidence for intensive magmatism immediately before the end-Permian mass extinction. *Geology* **45**, 343–346 (2017).
21. Sun, H. et al. Rapid enhancement of chemical weathering recorded by extremely light seawater lithium isotopes at the Permian-Triassic boundary. *Proc. Natl. Acad. Sci. USA* **115**, 3782–3787 (2018).
22. Wu, H. et al. Time-calibrated Milankovitch cycles for the late Permian. *Nat. Commun.* **4**, 2452 (2013).
23. Yuan, D. X. et al. Revised conodont-based integrated high-resolution timescale for the Changhsingian Stage and end-Permian extinction interval at the Meishan sections, South China. *Lithos* **204**, 220–245 (2014).
24. Zhang, M. et al. Magnetostratigraphy across the end-Permian mass extinction event from the Meishan sections, southeastern China. *Geology* **49**, 1289–1294 (2021).
25. Roberts, A. P., Cui, Y. & Verosub, K. L. Wasp-waisted hysteresis loops: Mineral magnetic characteristics and discrimination of components in mixed magnetic systems. *J. Geophys. Res.: Solid Earth* **100**, 17909–17924 (1995).
26. Robertson, D. J. & France, D. E. Discrimination of remanence-carrying minerals in mixtures, using isothermal remanent magnetization acquisition curves. *Phys. Earth Planet. Inter.* **82**, 223–234 (1994).
27. Kruiver, P. P., Dekkers, M. J. & Heslop, D. Quantification of magnetic coercivity components by the analysis of acquisition curves of isothermal remanent magnetisation. *Earth Planet. Sci. Lett.* **189**, 269–276 (2001).
28. Bloemendal, J., King, J., Hall, F. & Doh, S. J. Rock magnetism of Late Neogene and Pleistocene deep-sea sediments: Relationship to sediment source, diagenetic processes, and sediment lithology. *J. Geophys. Res.: Solid Earth* **97**, 4361–4375 (1992).
29. Tadić, M. et al. Synthesis, morphology, microstructure and magnetic properties of hematite submicron particles. *J. Alloys Compd.* **509**, 7639–7644 (2011).
30. Kosmulski, M., Durand-Vidal, S., Mączka, E. & Rosenholm, J. B. Morphology of synthetic goethite particles. *J. Colloid Interface Sci.* **271**, 261–269 (2004).
31. Dunlop, D. J. & Özdemir, Ö. *Rock Magnetism: Fundamentals and Frontiers*. (Cambridge University Press, 1997).
32. Song, H. et al. Geochemical evidence from bio-apatite for multiple oceanic anoxic events during Permian–Triassic transition and the link with end-Permian extinction and recovery. *Earth Planet. Sci. Lett.* **353-354**, 12–21 (2012).
33. Roberts, A. P. Magnetic mineral diagenesis. *Earth Sci. Rev.* **151**, 1–47 (2015).
34. Algeo, T. J. & Twitchett, R. J. Anomalous Early Triassic sediment fluxes due to elevated weathering rates and their biological consequences. *Geology* **38**, 1023–1026 (2010).
35. Song, H. et al. Integrated Sr isotope variations and global environmental changes through the Late Permian to early Late Triassic. *Earth Planet. Sci. Lett.* **424**, 140–147 (2015).
36. Burgess, S. D. & Bowring, S. A. High-precision geochronology confirms voluminous magmatism before, during, and after Earth's most severe extinction. *Sci. Adv.* **1**, e1500470 (2015).
37. Shen, S. Z. et al. A sudden end-Permian mass extinction in South China. *Geol. Soc. Am. Bull.* **131**, 205–223 (2019).
38. Jin, Y. et al. The Global Boundary Stratotype Section and Point (GSSP) for the base of Changhsingian Stage (Upper Permian). *Episodes* **29**, 175–182 (2006).
39. Zhang, K. & Shields, G. A. Sedimentary Ce anomalies: Secular change and implications for paleoenvironmental evolution. *Earth Sci. Rev.* **229**, 104015 (2022).
40. Liu, X.-M., Hardisty, D. S., Lyons, T. W. & Swart, P. K. Evaluating the fidelity of the cerium paleoredox tracer during variable carbonate

diagenesis on the Great Bahamas Bank. *Geochim. Cosmochim. Acta* **248**, 25–42 (2019).

41. Banner, J. L., Hanson, G. N. & Meyers, W. J. Rare earth element and Nd isotopic variations in regionally extensive dolomites from the Burlington-Keokuk Formation (Mississippian); implications for REE mobility during carbonate diagenesis. *J. Sediment. Res.* **58**, 415–432 (1988).

42. Liu, X.-M. et al. A persistently low level of atmospheric oxygen in Earth's middle age. *Nat. Commun.* **12** https://doi.org/10.1038/s41467-020-20484-7 (2021).

43. Bolhar, R. & Van Kranendonk, M. J. A non-marine depositional setting for the northern Fortescue Group, Pilbara Craton, inferred from trace element geochemistry of stromatolitic carbonates. *Precambrian Res* **155**, 229–250 (2007).

44. Frimmel, H. E. Trace element distribution in Neoproterozoic carbonates as palaeoenvironmental indicator. *Chem. Geol.* **258**, 338–353 (2009).

45. Tostevin, R. et al. Effective use of cerium anomalies as a redox proxy in carbonate-dominated marine settings. *Chem. Geol.* **438**, 146–162 (2016).

46. Li, M. et al. Nickel isotopes link Siberian Traps aerosol particles to the end-Permian mass extinction. *Nat. Commun.* **12**, 1–7 (2021).

47. Jin, Y. G. et al. Pattern of marine mass extinction near the Permian-Triassic boundary in South China. *Science* **289**, 432–436 (2000).

48. Wang, Y. et al. Quantifying the process and abruptness of the end-Permian mass extinction. *Paleobiology* **40**, 113–129 (2014).

49. Wei, H., Tang, Z., Yan, D., Wang, J. & Roberts, A. P. Guadalupian (Middle Permian) ocean redox evolution in South China and its implications for mass extinction. *Chem. Geol.* **530**, 119318 (2019).

50. Fielding, C. R. et al. Age and pattern of the southern high-latitude continental end-Permian extinction constrained by multiproxy analysis. *Nat. Commun.* **10**, 1–12 (2019).

51. Gastaldo, R. A. et al. The base of the Lystrosaurus Assemblage Zone, Karoo Basin, predates the end-Permian marine extinction. *Nat. Commun.* **11**, 1–8 (2020).

52. Chu, D. et al. Metal-induced stress in survivor plants following the end-Permian collapse of land ecosystems. *Geology* **49**, 657–661 (2021).

53. Fielding, C. R. et al. Sedimentology of the continental end-Permian extinction event in the Sydney Basin, eastern Australia. *Sedimentology* **68**, 30-62 (2021).

54. Chapman, T., Milan, L. A., Metcalfe, I., Blevin, P. L. & Crowley, J. Pulses in silicic arc magmatism initiate end-Permian climate instability and extinction. *Nat. Geosci.* **15**, 411–416 (2022).

55. Grasby, S. E., Sanei, H. & Beauchamp, B. Catastrophic dispersion of coal fly ash into oceans during the latest Permian extinction. *Nat. Geosci.* **4**, 104–107 (2011).

56. Sobolev, S. V. et al. Linking mantle plumes, large igneous provinces and environmental catastrophes. *Nature* **477**, 312–316 (2011).

57. Zhang, H. et al. Felsic volcanism as a factor driving the end-Permian mass extinction. *Sci. Adv.* **7**, eabh1390 (2021).

58. Shen, J., Zhang, Y. G., Yang, H., Xie, S. & Pearson, A. Early and late phases of the Permian–Triassic mass extinction marked by different atmospheric CO2 regimes. *Nat. Geosci.* **15**, 1–6 (2022).

59. Wu, Y. et al. Six-fold increase of atmospheric pCO2 during the Permian–Triassic mass extinction. *Nat. Commun.* **12**, 2137 (2021).

60. Penn, J. L., Deutsch, C., Payne, J. L. & Sperling, E. A. Temperature-dependent hypoxia explains biogeography and severity of end-Permian marine mass extinction. *Science* **362**, eaat1327 (2018).

61. Schobben, M. et al. A nutrient control on marine anoxia during the end-Permian mass extinction. *Nat. Geosci.* **13**, 640–646 (2020).

62. Haslett, J. & Parnell, A. A simple monotone process with application to radiocarbon-dated depth chronologies. *J. Royal Stat. Soc. Series C. Appl Stat* **57**, 399–418 (2008).

63. Parnell, A. C., Haslett, J., Allen, J. R. M., Buck, C. E. & Huntley, B. A flexible approach to assessing synchroneity of past events using Bayesian reconstructions of sedimentation history. *Quat. Sci. Rev.* **27**, 1872–1885 (2008).

64. Strehlau, J. H., Hegner, L. A., Strauss, B. E., Feinberg, J. M. & Penn, R. L. Simple and efficient separation of magnetic minerals from speleothems and other carbonates. *J. Sediment. Res.* **84**, 1096–1106 (2014).

65. Jenner, G. A., Longerich, H. P., Jackson, S. E. & Fryer, B. J. ICP-MS — A powerful tool for high-precision trace-element analysis in Earth sciences: Evidence from analysis of selected U.S.G.S. reference samples. *Chem. Geol.* **83**, 133–148 (1990).

66. Taylor, S. R. & McLennan, S. M. *The continental crust: Its composition and evolution*. 1–312 (Blackwell Scientific Pub.,Palo Alto, CA, 1985).

67. Pourmand, A., Dauphas, N. & Ireland, T. J. A novel extraction chromatography and MC-ICP-MS technique for rapid analysis of REE, Sc and Y: Revising CI-chondrite and Post-Archean Australian Shale (PAAS) abundances. *Chem. Geol.* **291**, 38–54 (2012).

68. Lécuyer, C. et al. δ18O and REE contents of phosphatic brachiopods: a comparison between modern and lower Paleozoic populations. *Geochim. Cosmochim. Acta* **62**, 2429–2436 (1998).

69. Blakey, R.C. Triassic global paleogeographic map (250 Ma). Global Paleogeography and Tectonics in Deep Time Series (*Deep Time Maps™,*2020). https://deeptimemaps.com/map-lists-thumbnails/global-paleogeography-and-tectonics-in-deep-time/.

Author contributions

M.Z., Y.-X.P. and S.-Z.S. conceptualized the research. H.Q., K.H., Y.H. and M.Z. performed the sampling. M.Z. performed the experiments. C.D., M.Z., H.Q. and Y.-X.P. analyzed the data. M.Z., Y-X.P. and S.-Z.S. wrote the manuscript and supplementary material. All authors supported the writing and editing process.

Competing interests

The authors declare no competing interests.

Additional information

Supplementary information The online version contains supplementary material available at https://doi.org/10.1038/s43247-024-01394-8.

Correspondence and requests for materials should be addressed to Min Zhang.

Peer review information *Communications Earth and Environment* thanks Christopher R Fielding, Michiel de Kock and the other, anonymous, reviewer(s) for their contribution to the peer review of this work. Primary Handling Editors: Carolina Ortiz Guerrero. A peer review file is available.

Reprints and permissions information is available at http://www.nature.com/reprints